Available online at www.sciencedirect.com

ScienceDirect

Proceedings of the Combustion Institute 35 (2015) 3471–3478

Proceedings of the Combustion Institute

www.elsevier.com/locate/proci

Nanosecond plasma enhanced $H_2/O_2/N_2$ premixed flat flames

Sharath Nagaraja [a], Ting Li [b], Jeffrey A. Sutton [b], Igor V. Adamovich [b], Vigor Yang [a,*]

[a] School of Aerospace Engineering, Georgia Institute of Technology, Atlanta, GA 600036, United States
[b] Department of Mechanical and Aerospace Engineering, Ohio State University, Columbus, OH 43210, United States

Available online 16 September 2014

Abstract

The effect of nanosecond pulsed plasma discharges on a laminar, lean ($\phi = 0.5$) premixed $H_2/O_2/N_2$ flame is studied at low pressure (25 Torr) using a novel plasma–flame facility, non-intrusive laser diagnostics, and high-fidelity numerical simulations. Spatially-resolved, quantitative OH mole fraction and temperature measurements are performed with and without a burst of 200 discharge pulses using laser-induced fluorescence. Measured temperatures increase by ~20% in both the pre-heat and post-flame zones with the use of the plasma discharge. In addition, OH mole fractions increase by as much as 500% in the preheat zone and by 40% in the post-flame gases. Simulations are conducted with a one-dimensional, multi-scale, pulsed-discharge model with detailed plasma-combustion kinetics to develop additional insight into the complex plasma and flame interactions. Good agreement between measured and predicted OH and temperature profiles provides confidence in the model framework. The reduced electric field, E/N, varies inversely with number density during each pulse. A significant fraction of the input energy is consumed during electron impact ionization processes in the high E/N (700–1000 Td) regions downstream of the flame. Lower E/N values (100–700 Td) in the lower-temperature preheat zone promote efficient generation of radicals and excited species via electron impact processes, as well as by collisional quenching of excited states. The plasma action results in a significant increase in O and H atom density, with the peak values increasing by a factor of 6 and 4 respectively. In presence of the discharge, species and temperature profiles shift upstream (closer to the burner) by approximately 0.2 cm. Simulations show that electron impact dissociation and excitation processes in the plasma have a major impact on the observed temperature and species profile displacement, such that Joule heating alone does not account for the observed effects of the plasma.

Keywords: Plasma-assisted combustion; Nanosecond plasma discharge; Burner stabilized premixed flame; Plasma fluid modeling; Laser induced fluorescence

1. Introduction

In recent years, non-equilibrium plasma discharges have received considerable attention

* Corresponding author.
E-mail address: vigor@gatech.edu (V. Yang).

http://dx.doi.org/10.1016/j.proci.2014.08.024
1540-7489/

for enhancement of ignition and flame stabilization in a variety of combustion systems [1]. High values of local electric field to number density ratio (E/N) in nanosecond discharges [1,2], in the range of 100–1000 Td (1 Td = 10^{-17} V-cm^2), allows for efficient generation of radicals and excited species via electron impact reactions, which can kinetically enhance the ignition and flame stabilization processes.

Previous experimental and numerical investigations have been conducted to understand the role of plasma-generated species in ignition [3–6], flame speed enhancement [7], and flame stabilization and extinction [8–11]. Recent studies on ignition of mildly-preheated (473–500 K) H_2–air mixtures [3,4] subjected to pulsed nanosecond plane-to-plane dielectric barrier discharges demonstrated that ignition kernel growth was an order of magnitude faster than the heat transport rates. The local plasma chemistry effects brought the mixture to the ignition threshold, resulting in nearly simultaneous ignition in the discharge volume.

Sun et al. [8] showed that *in situ* generated nanosecond plasma had a significant effect on the ignition–extinction characteristics of CH_4/He/O_2 counterflow diffusion flames, replacing the conventional S-curve with a new monotonic stretched ignition curve. Michael et al. [10] found that short microwave pulse bursts could increase the CH_4–air laminar flame speed by up to 25% and decrease the lean flammability limit by a factor of two. The significant temperature increase from the microwave coupling suggested a strong thermal mechanism for the observed enhancement of the flame properties. In general, however, due to the complexity of the interaction between plasma and flame kinetics, the fundamental enhancement mechanisms are poorly understood.

Recently, Li et al. [11] developed a burner platform to study the coupling between laminar, low-pressure, premixed flames and *in situ* generated nanosecond plasma discharges. The combination of diffuse plasma and a steady, laminar, quasi-one-dimensional flame in this configuration is conducive to both laser-based measurements and numerical modeling with detailed kinetic mechanisms. In the present work, we investigate the effect of pulsed nanosecond discharges on a lean ($\phi = 0.5$), premixed $H_2/O_2/N_2$ flame operating at 25 Torr with the burner platform described in [11]. Spatially-resolved OH and temperature measurements are performed with and without a burst of 200 discharge pulses. A self-consistent, one-dimensional numerical model [4,12] capable of resolving electric field transients over nanosecond timescales (during each discharge pulse) and radical kinetics and transport processes occurring at micro-to-millisecond timescales is used to develop insight into the complex plasma/flame interactions. Particular efforts are made to understand the role of thermal vs kinetic effects of the plasma on the laminar premixed flame. In Michael et al. [10], the microwave energy was coupled only to the high-temperature, weakly-ionized reaction zone, where key heat release reactions were already near completion. We believe the present approach is more likely to affect combustion chemistry, since the non-equilibrium, nanosecond discharge pulses couple energy to the low-temperature preheat zone to generate radical species (O, H, and OH) before the majority of the energy release occurs.

2. Experimental details

2.1. Plasma–flame facility

The plasma–flame facility has been described in detail elsewhere [11], so only a brief overview is given here. A water-cooled, 6-cm-diameter McKenna burner [13] is housed within a low-pressure chamber (Fig. 1(a)) capable of achieving stable (combusting) operating conditions down to 5 Torr. The McKenna burner produces a steady, laminar, quasi-one-dimensional flame, which is conducive to both laser-based measurements and numerical modeling with detailed kinetic mechanisms. The flow rates of the gases are monitored using calibrated mass flow controllers and the pressure within the chamber is maintained at 25 Torr by a throttled vacuum pump (Welch 1397). In addition, the entire burner facility can be translated in the vertical direction with a resolution of 3 μm to facilitate spatially-resolved laser-based measurements as a function of height above the burner surface.

In the configuration referred to as "direct flame coupling" (DFC), the entire combustion process (preheating, high-temperature reaction zone, and products) is encapsulated within the plasma

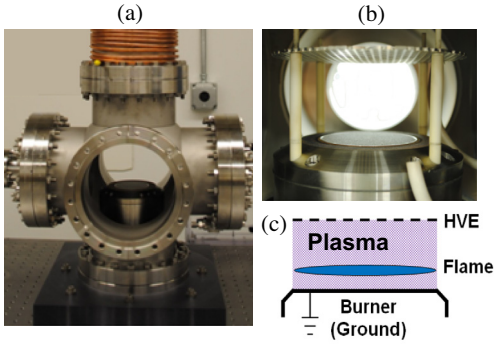

Fig. 1. (Left to right) (a) Photograph of plasma–flame facility; (b) photograph of McKenna burner and high-voltage electrode; (c) schematic of the "Direct Coupling" configuration.

discharge, as shown in Fig. 1(b). The burner surface acts as the ground electrode, and the high-voltage electrode is a 12-cm-diameter Tungsten mesh (open area = 90%) located 40 mm above the burner surface, which is supported by four ceramic posts mounted to the outer portion of the McKenna burner (see Fig. 1(b)). This location of the high-voltage electrode results in direct coupling of the plasma processes to the combustion chemistry of interest, while providing minimal disturbance to the laminar flow field. As shown in [11], the uniformity of the large-volume plasma discharge under the low-pressure and high-temperature conditions of the plasma–flame facility is quite good.

2.2. OH laser-induced fluorescence measurements

Figure 2 shows a schematic of the OH LIF diagnostic system that is used to measure temperature and quantitative OH mole fractions in the low-pressure plasma/flame facility. A digital delay generator (Stanford Systems DG 645) serves as the "master clock" for the entire system, sending a 10 Hz signal to an Nd:YAG laser system and the nanosecond-pulsed plasma generator. The second harmonic output of the Nd:YAG laser (Spectra-Physics Indi-40-10) operating at 532 nm is used to pump a tunable dye laser (Sirah Cobra-Stretch) to generate wavelengths in the vicinity of 562 nm. The visible output near 562 nm is frequency-doubled using a type-I BBO crystal to generate tunable ultraviolet output near 281 nm, which can excite rotational transitions within the (1,0) band of OH $A^2\sum^+$–$X^2\Pi$ system. The combination of a half wave plate and a thin film polarizer is used to attenuate the laser energy to less than 0.4 μJ/pulse to avoid saturation of the excited transitions. The UV laser beam then passes through a 500 μm-diameter pinhole, which defines the spatial resolution of the measurements in the direction normal to laser propagation, and passes into the vacuum chamber through a fused silica laser window oriented near Brewster's angle to minimize reflections.

For low laser pulse energies, the fluorescence signal is expressed as

$$S_{fl} = n_{OH}\frac{B_{12}}{c}\frac{E}{\Delta\nu_L}f_B\Gamma\phi F_{fl}l\frac{\Omega}{4\pi}\varepsilon\eta \quad (1)$$

where n_{OH} is the number density of OH, B_{12} is the Einstein absorption coefficient, c is the speed of light, E is the laser energy, $\Delta\nu_L$ is the laser linewidth, f_B is the Boltzmann fraction, Γ is the dimensionless overlap integral between the laser and the absorption lineshapes, ϕ is the fluorescence quantum yield, F_{fl} is the fraction of fluorescence bandwidth collected, l is the laser path length sampled by the collection optics, ε is the efficiency of the optical system, and η is the efficiency of the detection system. The fluorescence emitted from the center of the flame is collected and focused onto a photo-multiplier tube (PMT; Hamamatsu R9220) by a set of two plano-convex spherical lenses. Schott glass BG3 and UG11 optical filters are placed in front of the PMT in order to block the broadband flame and plasma emission and allow only the collection of the OH LIF emission. The individual pulse-to-pulse energy fluctuations are monitored with a fast-response photodiode (Thorlabs DET10A; rise time of 1 ns). Both the OH fluorescence signal and the relative laser energies (photodiode signals) are collected on a digital oscilloscope (Lecroy Wave Runner 104Xi-A; 1 GHz bandwidth). To determine quantitative OH measurements from

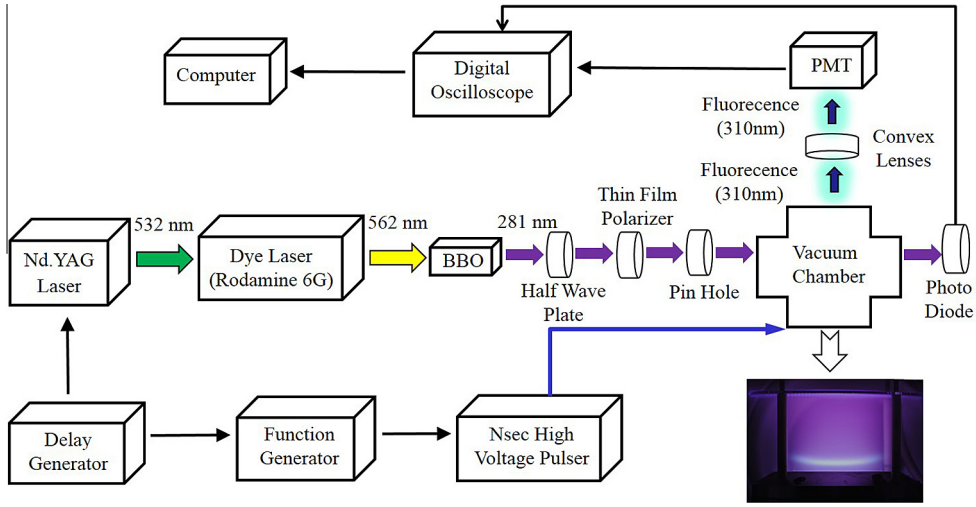

Fig. 2. Schematic of the coupled OH laser induced fluorescence system and low-pressure plasma/flame facility.

measured LIF signals, the fluorescence quantum yield is defined as $\phi = \tau_{fl}/\tau_{rad}$, where τ_{fl} is the measured fluorescence lifetime and τ_{rad} is the collision-free radiative lifetime taken from German [14]. The fluorescence lifetime is determined by fitting the measured fluorescence signal to a single exponential decay. The effect of plasma on the quenching rate is found to be small (<10% difference). For the spatially-resolved measurements, only one time delay ($\Delta t = 8$ μs) between the plasma discharge and the Nd:YAG laser is reported. This Δt corresponds to the time delay after which the largest increase of OH (due to the presence of the plasma) is measured and the plasma emission (e.g., N2(C-B)) has completely decayed. All of the experiments described here are performed with 200 pulses in the burst and each OH fluorescence measurement is collected (or averaged) over 10 ns.

Spatially-resolved temperature profiles are measured by recording OH LIF profiles for five rotational states of the OH $A^2\sum^+ \leftarrow X^2\prod$ ($v' = 1$, $v'' = 0$) transition: R1(8), R1(9), R1(10), R1(11), R1(13). For each spatial position (in 500 μm steps), the measured intensity is plotted against the rotational energy in a Boltzmann plot to determine the temperature. Two hundred laser shots (and hence fluorescence waveforms) are recorded at each location. The relative OH LIF signals from the R1(9) rotational line are converted to relative OH mole fraction profiles by correcting the LIF signals for pulse energy, temperature, Boltzmann fraction, and overlap integral variations as a function of height above the burner. The relative OH mole fraction profiles are placed on an absolute scale by normalizing the profiles by an LIF measurement in a well-characterized $\phi = 1.07$ $CH_4/O_2/N_2$ flame at a height of 1.2 cm above the burner surface. At 1.2 cm above the burner, the absolute OH mole fraction is determined with a laser absorption measurement. For the absorption measurement, the laser system is tuned to the Q1(10) rotational line within OH $A^2\sum^+ \leftarrow X^2\prod$ ($v' = 0$, $v'' = 0$) transition near 309.5 nm, and the measured mole fraction of 0.0104 is within 7% of previously-published results for the same flame [15].

The uncertainty (in terms of precision) of the temperature measurements is primarily due to finite signal-to-noise ratio (SNR) considerations. Lower SNR of high rotational levels introduces a 10% (±100 K) uncertainty at low temperatures (800–1000 K). At temperatures greater than 1000 K, the uncertainty decreases to approximately 3% (±50 K). To a large extent, we avoid the temperature influence on OH measurements by using line R1(9). Quantification of the OH LIF signal, however, requires several temperature-dependent considerations, including the Boltzmann population, electronic quenching due to other species, and the overlap of the laser frequency with the Doppler-broadened OH absorption transition. Uncertainty is also introduced when the relative OH profiles are placed on an absolute scale using direct absorption. All of these considerations lead to an estimated uncertainty of 20% in the absolute OH concentration measurements.

3. Numerical framework

In order to obtain more insight into the multi-scale interactions between the laminar flame and nanosecond pulsed discharges, one-dimensional, self-consistent simulations are performed with detailed chemistry. The details of the numerical framework are described elsewhere [4,12]. Briefly, equations for electric potential, electron energy, and charged and neutral-species continuity are considered. In addition, continuity, momentum and gas temperature equations are solved. The electron transport and reaction coefficients are expressed as functions of electron energy using predictions of a Boltzmann equation solver, BOLSIG [16], and updated at every time step through interpolation. The mixture-averaged formulation from the CHEMKIN package [17] is used to obtain thermal conductivities and diffusion coefficients.

A non-uniform mesh consisting of 600 grid points is used to obtain grid-converged solutions, with high resolution near the flame location and close to the electrodes. Temperature, velocity, and species mole fractions are specified at the inlet. A vanishing gradient boundary condition is applied for the energy equation, whereas species mole fractions are extrapolated at the outlet. Charged-species fluxes include a drift component (due to electric field), and electron flux at the cathode boundary includes a contribution from secondary emission.

A simulation is performed at 25 Torr with the discharge pulser switched off (no plasma) to

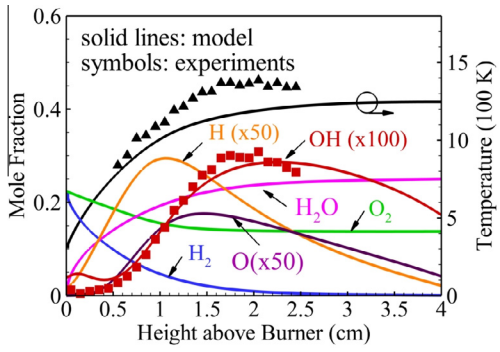

Fig. 3. Steady-state temperature and species concentration distributions as functions of height above the burner for a $H_2/O_2/N_2$ ($\phi = 0.5$) flame at 25 Torr, with plasma discharge switched off.

obtain a steady-state flame solution, as shown in Fig. 3. Mole fractions of H_2, O_2 and N_2 at the inlet are 0.2327, 0.2327 and 0.5346 respectively (obtained from the experimental operating conditions). The temperature and velocity at the inlet are fixed at $T_{in} = 345$ K and $u_{in} = 0.36$ m/s respectively. The model predictions are sensitive to the inlet and outlet boundary conditions. An inlet temperature of 345 K is used in the simulations, since it provides the best match between the predicted and measured baseline flame temperature profiles. Spatially-resolved OH and temperature data from the experiments, also shown in Fig. 3, compare well with the predictions, validating the transient flame model without the plasma.

The flame solution in Fig. 3 provides initial neutral species and temperature distributions for the pulsed-discharge simulations. The charged-species mole fractions are initialized to 1×10^{-10}, except for electron density fraction, which is initially fixed at 6×10^{-10} to ensure charge neutrality. Owing to the pulsed nature of the discharge process considered in this work, photoionization is not important and residual electrons from previous pulses provide seed electrons for initiation of the next pulse. The predictive capability of the present numerical code has been validated previously for pulsed nanosecond discharges in air [12] and H_2–air mixtures [4].

3.1. $H_2/O_2/N_2$ plasma flame chemistry

A detailed kinetics mechanism consisting of 42 species and 310 reactions is compiled by combining $H_2/O_2/N_2$ plasma chemistry data [18–19] with conventional H_2–O_2 combustion kinetics [19–20] and NO_x kinetics [21–22]. The mechanism incorporates charged species O^+, N_2^+, O_2^+, N_4^+, O_4^+, H_2^+, H_3^+, HN_2^+, HO_2^+, H_2O^+, H_3O^+, O^-, O_2^-, e^-; excited species $N_2(A^3\Sigma)$, $N_2(B^3\Pi)$, $N_2(C^3\Pi)$, $N_2(a'^1\Sigma)$, $N(^2D)$, $O_2(a^1\Delta)$, $O_2(b^1\Sigma)$, $O_2(c^1\Sigma)$, $O(^1D)$; and neutral species N_2, H_2, O_2, H, O, N, O_3, OH, HO_2, H_2O_2, H_2O, NO, NO_2, NH, NNH, NH_2, NH_3, N_2O HNO. The plasma chemistry processes pertaining to H_2O (such as ionization and dissociation) also have been included, since they are important in accurately predicting the discharge development downstream of the flame. The present model does not incorporate vibrational excitation by electron impact and vibrational energy transfer processes. Our previous results [4] demonstrated that vibrational non-equilibrium in plane-to-plane nanosecond pulse discharges in air and H_2–air is insignificant.

4. Results and discussion

The experiments make use of a high-voltage, short-duration fast ionization dynistor (FID) plasma generator. Voltage and current pulse shapes during pulser operation are measured with a Tektronix P6015A high-voltage probe and Pearson current monitor (model 2877), and are shown in Fig. 4. The pulse width, as defined by the full width at half maximum (FWHM) value, is approximately 7 ns and the estimated pulse energy is 3 mJ/pulse, which is independent of the flame conditions. We observe a delay between the voltage and the current, with the latter achieving a peak value of ~60 A, nearly 6 ns after the voltage reaches its maximum value. The curve fit corresponding to the FID voltage waveform used in the simulations, and the calculated current, also are shown in Fig. 4. As shown in Fig. 4, the model is able to accurately predict the shape of the current pulse, although it under-predicts the peak value by 20%. The predicted coupled energy is 3.4 mJ per pulse, which is close to the value calculated from the voltage and current measurements. In the experiment, in addition to the main pulse, there are several reflected pulses that couple additional energy, but it is significantly less than the energy coupled by the main discharge pulse (<15% of the main pulse).

Figure 5 shows the model predictions of electron number density and reduced electric field (E/N) as a function of space and time during a discharge pulse in the presence of a lean, premixed $H_2/O_2/N_2$ flame. The inlet conditions and initial flame conditions (without plasma) are the same as in Fig. 3. The E/N profiles are similar to that of temperature, with lower values in the pre-heat zone because of higher number density. The E/N attains much higher values (up to 1500 Td) for a short duration near the post-flame boundary because of the cathode sheath formation. A significant portion of the input energy is consumed in electron-impact ionization in the high-temperature, post-flame gases because of high E/N (700–1000 Td). Due to the lower temperatures near the burner and in the preheating zone, input

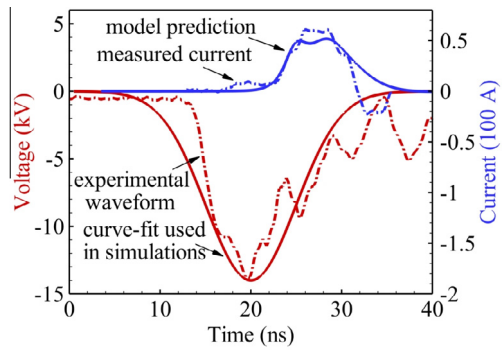

Fig. 4. FID voltage and current waveforms measured at the high voltage electrode; voltage curve-fit used in the simulations and predicted current at 25 Torr in a $H_2/O_2/N_2$ ($\phi = 0.5$) flame.

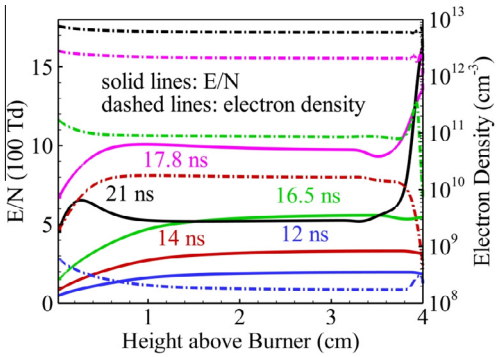

Fig. 5. Spatial distributions of reduced electric field, E/N, and electron number density during a FID voltage pulse predicted by the model at 25 Torr in a $H_2/O_2/N_2$ ($\phi = 0.5$) flame.

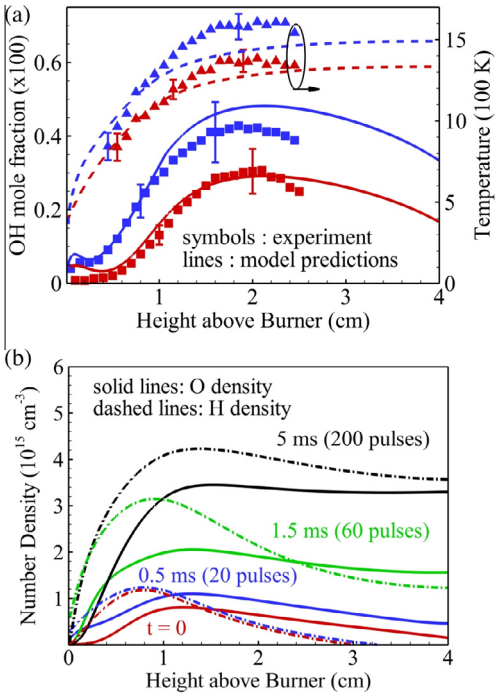

Fig. 6. (a) Measured and predicted OH concentration and temperature (squares – OH mole-fraction, triangles – temperature; red – without plasma, blue – with plasma), (b) predicted O and H densities as a function of height above burner before and after a burst of 200 FID pulses at 25 Torr in a $H_2/O_2/N_2$ ($\phi = 0.5$) flame.(For interpretation of the references to color in this figure legend, the reader is referred to the web version of this article.)

energy is coupled at E/N values of 100–700 Td, resulting in efficient generation of radicals and excited species via electron impact dissociation and excitation processes, as well as quenching of excited electronic states of N_2. The electron density evolves in a spatially-uniform manner, with a peak value of $\sim 7 \times 10^{12}$ cm^{-3} attained at ~21 ns.

Figure 6(a) shows spatially-resolved OH density and temperature measurements as a function of height above the burner surface, with and without the application of 200 discharge pulses at a 40 kHz repetition rate. A significant increase in OH concentration is observed after the pulse burst, with a 40% increase in the peak mole fraction from 0.003 to 0.004 at 2 cm location above the burner. The plasma effect also results in an approximately 20% rise in temperature in the burnt-gas region. While the temperature rise in the preheat zone (0.5–1.5 cm above the burner surface) is similar (20%), the increase in OH mole fraction is substantially higher. The OH mole fraction increases from 0.001 to 0.0025 at 9 mm above the burner surface, for example, which corresponds to an increase of 140%. Larger increases are observed closer to the burner surface.

Numerical simulations are performed to gain further insight into the plasma flame interactions. A burst of 200 FID pulses applied at 40 kHz repetition rate are simulated at the same operating conditions as in the experiments. The predicted temperature and OH profiles also are shown in Fig. 6(a). The inlet conditions and initial flame conditions (i.e., without plasma) are the same as in Fig. 3. The model performs well in predicting the OH mole fraction and temperature rise in the pre-heat zone. In the burnt-gas regions, OH concentration is over-predicted, whereas the calculated temperatures are ~10% below the measured values. The trend is, however, correctly predicted in both cases, giving confidence in utilizing the model framework to investigate the plasma and flame interactions.

Figure 6(b) shows the spatial distribution of O and H radicals predicted by the model at various points in time during the 200 pulse simulation. A significant rise in species concentrations is observed because of the pulsed discharge processes, with peak values of H and O increasing by approximate factors of four and six, respectively. It is interesting to note that the gradients of radical concentrations and temperature are substantially higher in the pre-heat zone in the presence of the pulsed discharge. This suggests that the plasma chemistry accelerates ignition, causing the species concentration profiles to shift upstream by approximately 0.2 cm. Figure 7 shows a path flux analysis quantifying the key production pathways of O, H and OH at 0.6 cm above the burner. A substantial fraction of O and H radicals are generated directly by dissociation of O_2 and H_2 molecules through collisions with high-energy electrons (electron impact) and excited N_2 species (dissociative quenching). On the other hand, OH is a secondary radical gener-

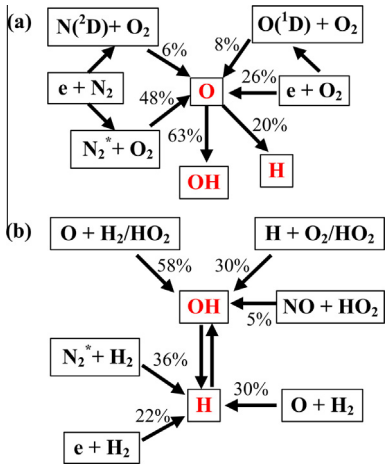

Fig. 7. Path flux analysis describing the major formation/destruction pathways of (a) O, (b) H and OH after a burst of 200 FID pulses at 0.6 cm location above the burner at 25 Torr in a $H_2/O_2/N_2$ ($\phi = 0.5$) flame. Percentage contributions of difference channels are indicated.

ated by reactions of O and H with HO_2, and other chain-branching reactions. Note that OH produced by the pulsed plasma triggers heat release by reactions of OH with H_2, to generate H_2O and H. The resultant increase in temperature accelerates the conventional H_2–O_2 chain branching processes, thereby creating a positive feedback loop for rapid production of radicals. At locations closer to the burner, lower temperatures aid in the formation of O_3 and HO_2 from O and H radicals, respectively. Ozone is transported a short distance downstream before it decomposes to O when the temperature rises above 500 K. HO_2 persists for a longer distance, until the temperature increases to about 700 K.

In the present configuration, the time-averaged discharge power during the burst is nearly 50% of the heat of combustion. Thus, it is not surprising that the pulsed-plasma source has a significant impact on flame properties. It is, however, critical to understand whether the plasma effect is predominantly thermal, or if non-equilibrium kinetics play an important role in modifying the flame structure. To determine this, we performed an additional simulation, considering only the Joule heating effect during each pulse and with the electron impact chemistry processes switched off. The Joule heating term is given by the following Eq. [23],

$$J_H = |e\vec{E} \cdot (\vec{\Gamma}_+ - \vec{\Gamma}_- - \vec{\Gamma}_e)| \qquad (2)$$

where $\vec{E}$ is the electric field, $\vec{\Gamma}_+$, $\vec{\Gamma}_-$, and $\vec{\Gamma}_e$ are the fluxes of positive ions, negative ions, and electrons, respectively, and e is the electron charge. This quantity was calculated as a function of space and time from electric field and flux data predicted by the pulsed discharge simulation in Fig. 6. JH is used as a source term in the gas temperature equation, while all electron impact processes are turned off during the discharge pulses. Figure 8 shows spatial distributions of temperature, as well as O, H, and OH number densities, after a burst of 200 discharge pulses with and without incorporating electron impact kinetics (in the latter case, only Joule heating is considered). The peak values of O and H densities decrease by nearly 30% when the non-equilibrium electron chemistry effects are not taken into account in the model. As seen in Fig. 6, adding pulsed plasma results in an increase of a factor of 4 and 6 in the O and H densities, respectively. We can therefore conclude that Joule heating is responsible for a significant fraction of the plasma enhancement of the flame. Non-equilibrium chemistry effects, however, are of critical importance in the lower-temperature regions upstream of the flame. It is evident that species and temperature gradients are less steep when only Joule heating effect is considered. Also, adding all discharge energy in the form of heat results in a 20% lower temperature, as compared with the case considering non-equilibrium chemistry effects. The difference in temperature can be attributed to the heat release triggered by partial oxidation of fuel molecules by the plasma-generated radicals. Joule heating alone cannot shift the temperature and species profiles as far upstream (that is, as close to the burner surface) as the pulsed plasma source of the same total power.

It is estimated from the simulation results that only ~10% of the total input energy per pulse (3.2 mJ), or approximately 5% of the combustion power in this experiment, is coupled in the preheat and reaction zones. A significant portion of the input energy (~90%) is coupled downstream of

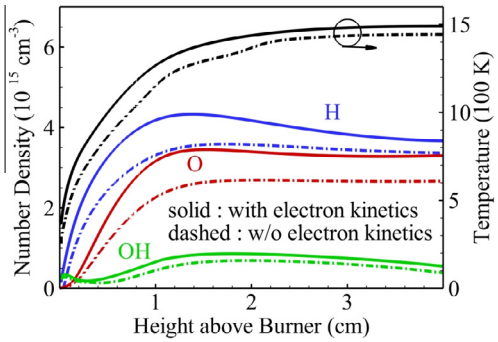

Fig. 8. Predicted O, H, and OH densities and temperature distributions as functions of height above the burner after a burst of 200 FID pulses, with and without incorporating electron impact kinetics into the model at 25 Torr in a $H_2/O_2/N_2$ ($\phi = 0.5$) flame.

the flame, which does not affect radical production in the preheat zone. Future work will focus on techniques to increase the energy coupled in the pre-heat zone by placing a high-voltage electrode (made of tungsten for high heat resistance) closer to the flame.

5. Conclusion

A novel plasma–flame facility has been developed to study the direct coupling of steady, laminar, low-pressure, premixed flames to highly non-equilibrium, nanosecond-pulsed plasma discharges. OH LIF diagnostics were used to measure temperature and quantitative OH mole fraction profiles, with high spatial resolution. The measurements were performed with and without a burst of 200 ns discharge pulses to quantify the effect of non-equilibrium plasma on a pre-existing lean premixed $H_2/O_2/N_2$ ($\phi = 0.5$) flame. Temperature increased by approximately 20% at all spatial locations and OH mole fraction increased by 100–500% in the preheat region and 40% in the post-flame gases due to the application of discharge pulses. A one-dimensional, multi-scale, pulsed-discharge modeling framework with detailed plasma combustion kinetics was used to develop additional insight into the complex plasma–flame interactions. Simulation results showed a significant increase in O and H densities due to plasma chemistry, with peak values increasing by factors of six and four, respectively. It was demonstrated that Joule heating alone cannot shift the temperature and species profiles as far upstream (as close to the burner surface) as the pulsed plasma source of the same total power.

The present experiments and modeling demonstrate two major, critical phenomena, not reported previously: (i) low-temperature plasma generates considerably higher amounts of O, H, and OH radicals in the preheat zone, compared to indiscriminate heating of the flow at the same rate, resulting in significant upstream displacement of the reaction zone at low plasma power (~5% of combustion power), and (ii) the effect of plasma chemistry on the flame is more pronounced at fuel-lean conditions.

Acknowledgments

This work was supported by MURI research grant FA9550-07-1-0136 from the Air Force Office of Scientific Research with Dr. Chiping Li as the technical monitor.

References

[1] S.M. Starikovskaia, *J. Phys. D: Appl. Phys.* 39 (16) (2006) R265–R299.
[2] Y.P. Raizer, *Gas Discharge Physics*, Springer, Barcelona, Spain, 1991.
[3] Z. Yin, I.V. Adamovich, W.R. Lempert, *Proc. Combust. Inst.* 34 (2013) 3249–3258.
[4] S. Nagaraja, V. Yang, Z. Yin, I.V. Adamovich, *Combust. Flame* (2013).
[5] I.N. Kosarev, N.L. Aleksandrov, S.V. Kindysheva, S.M. Starikovskaia, A. Yu Starikovskii, *Combust. Flame* 156 (1) (2009) 221–233.
[6] C.D. Cathey, T. Tang, T. Shiraishi, T. Urushihara, A. Kuthi, M.A. Gundersen, *IEEE Trans. Plasma Sci.* 35 (6) (2007) 1664–1668.
[7] T. Ombrello, S.H. Won, Y. Ju, S. Williams, *Combust. Flame* 157 (2010) 1906–1915.
[8] W. Sun, S.H. Won, T. Ombrello, C. Carter, Y. Ju, *Proc. Combust. Inst.* 34 (1) (2013) 847–855.
[9] G. Pilla, D. Galley, D.A. Lacoste, F. Lacas, D. Veynante, C.O. Laux, *IEEE Trans. Plasma Sci.* 34 (6) (2006) 2471–2477.
[10] J.B. Michael, T.L. Chng, R.B. Miles, *Combust. Flame* 160 (2013) 796–807.
[11] T. Li, I.V. Adamovich, J.A. Sutton, *Combust. Sci. Technol.* 185 (2013) 990–998.
[12] S. Nagaraja, V. Yang, I.V. Adamovich, *J. Phys. D: Appl. Phys.* 46 (15) (2013) 155205.
[13] Holthius & Associates at www.flatflame.com.
[14] K.R. German, *J. Chem. Phys.* 63 (1975) 5252.
[15] P.A. Berg, D.A. Hill, A.R. Noble, G.P. Smith, J.B. Jeffries, D.R. Crosley, *Combust. Flame* 121 (2000) 223–235.
[16] G.J.M. Hagelaar, L.C. Pitchford, *Plasma Sources Sci. Technol.* 14 (4) (2005) 722.
[17] R. J. Kee, J. F. Grcar, M. D. Smooke, J. A. Miller, *PREMIX: a fortran program for modeling steady laminar one-dimensional premixed flames*, Sandia National Laboratories report, 1985.
[18] M. Uddi, N. Jiang, I.V. Adamovich, W.R. Lempert, *J. Phys. D: Appl. Phys.* 42 (7) (2009) 075205.
[19] N.A. Popov, *Plasma Phys. Rep.* 34 (5) (2008) 376–391.
[20] A.A. Konnov, *Combust. Flame* 152 (4) (2008) 507–528.
[21] G.P. Smith, D.M. Golden, M. Franklach, et al., GRI-Mech 3.0, 1999, available at www.me.berkeley.edu/gri_mech/.
[22] K. Takita, N. Abe, G. Masuya, Y. Ju, *Proc. Combust. Inst.* 31 (2) (2007) 2489–2496.
[23] S.O. Macheret, M.N. Shneider, R.B. Miles, *IEEE Trans. Plasma Sci.* 30 (3) (2002) 1301–1314.